Shock Waves (2009) 19:251–264
DOI 10.1007/s00193-009-0201-2

ORIGINAL ARTICLE

Transient three-dimensional startup side load analysis of a regeneratively cooled nozzle

Ten-See Wang

Received: 7 May 2008 / Revised: 30 January 2009 / Accepted: 7 April 2009 / Published online: 8 May 2009

Abstract The objective of this effort is to develop a computational methodology to capture the side load physics and to anchor the computed aerodynamic side loads with the available data by simulating the startup transient of a regeneratively cooled, high-aspect-ratio nozzle, hot-fired at sea level. The computational methodology is based on an unstructured-grid, pressure-based, reacting flow computational fluid dynamics and heat transfer formulation, and a transient inlet history based on an engine system simulation. Emphases were put on the effects of regenerative cooling on shock formation inside the nozzle, and ramp rate on side load reduction. The results show that three types of asymmetric shock physics incur strong side loads: the generation of combustion wave, shock transitions, and shock pulsations across the nozzle lip, albeit the combustion wave can be avoided with sparklers during hot-firing. Results from both regenerative cooled and adiabatic wall boundary conditions capture the early shock transitions with corresponding side loads matching the measured secondary side load. It is theorized that the first transition from free-shock separation to restricted-shock separation is caused by the Coanda effect. After which the regeneratively cooled wall enhances the Coanda effect such that the supersonic jet stays attached, while the hot adiabatic wall fights off the Coanda effect, and the supersonic jet becomes detached most of the time. As a result, the computed peak side load and dominant frequency due to shock pulsation across the nozzle lip associated with the regeneratively cooled wall boundary condition match those of the test, while those associated with the adiabatic wall boundary condition are much too low. Moreover, shorter ramp time results show that higher ramp rate has the potential in reducing the nozzle side loads.

Keywords Transient nozzle side loads · Regeneratively cooled nozzle · Shock pulsation · Shock transition · Combustion wave · Coanda effect

PACS 47.32.Ff Separated flows · 47.40.-x Compressible flows; shockwaves · 47.40.Nm Shock wave interactions and shock effects · 47.60.Kz Flows and jets through nozzles

Communicated by A. Hadjadj.

T.-S. Wang (✉)
Fluid Dynamics Branch, NASA Marshall Space Flight Center,
Huntsville, AL 35812, USA
e-mail: Ten-See.Wang-1@nasa.gov

List of symbols

C_1, C_2, C_3, C_μ	Turbulence modeling constants, 1.15, 1.9, 0.25, and 0.09
C_p	Heat capacity
D	Diffusivity
F_{yz}	Integrated force in the lateral direction
H	Total enthalpy
K	Thermal conductivity
k	Turbulent kinetic energy
p	Pressure
Q	Heat flux
T	Temperature
t	Time
u_i	Mean velocities in three directions
x	Cartesian coordinates
α	Species mass fraction
ε	Turbulent kinetic energy dissipation rate
θ	Energy dissipation contribution
μ	Viscosity
μ_t	Turbulent eddy viscosity (=$\rho C_\mu k^2/\varepsilon$)
Π	Turbulent kinetic energy production

ρ Density
σ Turbulence modeling constants
τ Shear stress
ω Chemical species production rate

Subscripts

r Radiation
t Turbulent flow
w Wall

1 Introduction

Nozzle side loads are potentially detrimental to the integrity and life of almost all launch vehicle engines in development. For example, side load problems have been found in J2 engine [1], Block-I space shuttle main engine (SSME) [2], and recently, the Fastrac engine [3]. More recently, the European Vulcain engine [4] and the Japanese LE-7A engine [5] have also experienced side load difficulties. A better understanding of the mechanisms that contribute to side loads during engine transient operations must be attained and the predictive ability of which has to be developed, in order to develop ways to reduce the side loads. Unfortunately, current level in understanding the nozzle side load physics is still limited and the design methods are mostly empirical. The lack of a predictive capability may result in system level failures, and ultimately reduced life and increased weight for new engine systems. Subsequently, a detailed, general predictive methodology based on the computational fluid dynamics (CFD) appears to be the most promising.

Since the physics leading to nozzle side load are transient in nature, it was suggested that only transient CFD analysis can simulate the highly time-varying phenomenon [6]. Two early transient numerical attempts [7,8] have been reported for SSME and J2S nozzles, respectively. Unfortunately, although both captured the nozzle hysteresis phenomenon that is considered to be one of the basic characteristics of liquid rocket engine nozzles, the axisymmetric assumption precludes the capturing of any asymmetric flows. In addition, the hysteresis phenomenon referred in those two efforts was measured by axial forces which have little to do with the side forces. That means only transient, three-dimensional (3-D) CFD analyses can simulate any asymmetric flow physics. Fortunately, as the computer hardware and computational methodologies advance, the affordability and reliability of transient 3-D nozzle computations increase. Recently, two transient 3-D CFD simulations for nozzles hot-firing at sea level have been reported. Yonezawa et al. [9] made the first 3-D CFD startup side load prediction for the LE-7, LE-7A and CTP50-R5-L nozzles, while Boccaletto and Lequette [10] followed with a study on the influence of film cooling for the Vulcain 2 engine.

To simulate such a complicated transient physics, many assumptions have to be made by both groups to facilitate the computation. However, all assumptions made may ultimately affect the computed physics and need to be carefully examined. The assumptions and results of Yonezawa et al. [9] are followed in here since enough details of the computed physics were reported therefore their association with the assumptions can be related. The comparisons of computed side loads with those of tests are also helpful. Qualitatively, their result captured most physics such as the shock transitions and shock oscillations inside the nozzle. However, quantitative results were less satisfactory. For example, only one side load jump of 30 kN was predicted for LE-7A engine, while two side load jumps were observed, with peak side measured at more than 200 kN. In addition, the Mach disk was not captured when the nozzle was flowing full, yet it was observed during the hot-fire test.

That degenerated Mach disk was probably caused by the coarseness of the grid in the plume region, as stated by Yonezawa et al. [9]. It was further speculated that some of their modeling assumptions, e.g., the frozen flow, constant specific heat and linear ramp rate may have modified the predicted physics. A series of two-dimensional (2-D) and axisymmetric numerical studies on the effects of those assumptions were performed [11], and it was found that combustion and ramp rate drastically affect the computed side load physics. Basically, combustion changes the species composition hence the local temperature and specific heat distributions, while ramp rate affects the flow residence time and in turn the reaction rate. Those two intertwining factors affect both the Mach disk shape and Mach disk flow propagation history, thereby influencing wall pressure distribution and side load magnitudes. Tomita et al. [12] also demonstrated recently the importance of combustion on side load physics in a subscale combustion test. Furthermore, since LE-7A nozzle has a regeneratively cooled section, it is speculated that the adiabatic wall assumption was inadequate for the regeneratively cooled wall. This is important since Nave and Coffey [1] observed that colder walls tend to retard flow separation, and two steady, 2-D CFD analyses [13,14] showed that thinner, cold wall boundary layer is less susceptible to separation than the thicker, hot boundary layer of an adiabatic wall.

The objective of this effort is to develop a computational methodology to capture the side load physics and benchmark the computed side load with available data from a regeneratively cooled, high aspect ratio, full scale SSME nozzle, hot-fired at sea level. This is accomplished by improving on the lessons learned from the assumptions made by Yonezawa et al. [9], based on an unstructured-grid, reacting, pressure-based CFD and heat transfer methodology. Finite-rate chemistry was turned on throughout the startup transient to properly consider the heat release and its effect on thermal fluid properties. An engine system simulation was used to obtain a nominal 5 s sequence to closely simulate the actual inlet history of a hot-fire test. Regeneratively cooled and adiabatic thermal wall boundary conditions were used to understand the effect of regenerative cooling on side load physics. A hybrid mesh anchored for axial force and wall heat transfer characteristics [15] was shown to be adequate for side force applications. Finally, since short residence time has been speculated to reduce the impact of certain shock evolutions, a third transient case was performed using a proportionately shortened 1 s sequence to demonstrate the effect of higher ramp rate on side load reduction.

2 Computational methodology

2.1 Computational fluid dynamics and heat transfer

The computational methodology is based on a multi-dimensional, finite-volume, viscous, chemically reacting, unstructured grid, and pressure-based fluid dynamics and heat transfer formulation. Time-varying transport equations of continuity, species continuity, momentum, total enthalpy, turbulent kinetic energy, and turbulent kinetic energy dissipation were solved using a time-marching sub-iteration scheme and are written as:

$$\frac{\partial \rho}{\partial t} + \frac{\partial}{\partial x_j}(\rho u_j) = 0 \tag{1}$$

$$\frac{\partial \rho \alpha_i}{\partial t} + \frac{\partial}{\partial x_j}(\rho u_j \alpha_i) = \frac{\partial}{\partial x_j}\left[\left(\rho D + \frac{\mu_t}{\sigma_\alpha}\right)\frac{\partial \alpha_i}{\partial x_j}\right] + \omega_i \tag{2}$$

$$\frac{\partial \rho u_i}{\partial t} + \frac{\partial}{\partial x_j}(\rho u_j u_i) = -\frac{\partial p}{\partial x_i} + \frac{\partial \tau_{ij}}{\partial x_j} \tag{3}$$

$$\begin{aligned}\frac{\partial \rho H}{\partial t} &+ \frac{\partial}{\partial x_j}(\rho u_j H) \\ &= \frac{\partial p}{\partial t} + Q_r + \frac{\partial}{\partial x_j}\left(\left(\frac{K}{C_p} + \frac{\mu_t}{\sigma_H}\right)\nabla H\right) \\ &\quad + \frac{\partial}{\partial x_j}\left(\left((\mu + \mu_t) - \left(\frac{K}{C_p} + \frac{\mu_t}{\sigma_H}\right)\right)\nabla\left(V^2/2\right)\right) + \theta\end{aligned} \tag{4}$$

$$\begin{aligned}\frac{\partial \rho k}{\partial t} &+ \frac{\partial}{\partial x_j}(\rho u_j k) \\ &= \frac{\partial}{\partial x_j}\left[\left(\mu + \frac{\mu_t}{\sigma_k}\right)\frac{\partial k}{\partial x_j}\right] + \rho(\Pi - \varepsilon)\end{aligned} \tag{5}$$

$$\begin{aligned}\frac{\partial \rho \varepsilon}{\partial t} &+ \frac{\partial}{\partial x_j}(\rho u_j \varepsilon) = \frac{\partial}{\partial x_j}\left[\left(\mu + \frac{\mu_t}{\sigma_\varepsilon}\right)\frac{\partial \varepsilon}{\partial x_j}\right] \\ &+ \rho\frac{\varepsilon}{k}\left(C_1\Pi - C_2\varepsilon + C_3\Pi^2/\varepsilon\right)\end{aligned} \tag{6}$$

A predictor and corrector solution algorithm was employed to provide coupling of the governing equations. A second-order central-difference scheme was employed to discretize the diffusion fluxes and source terms. For the convective terms, a second-order upwind total variation diminishing difference scheme was used. To enhance the temporal accuracy, a second-order backward difference scheme was utilized to discretize the temporal terms. Sub-iterations within a time step are used for driving the system of second-order time-accurate equations to convergence. The maximum number of sub-iterations is limited to 30. Details of the numerical algorithm can be found in References [15–18].

An extended k–ε turbulence model [19] was used to describe the turbulence. In addition to the original dissipation rate time scale (k/ε), an additional production range time scale (k/Π) was added to represent the energy transfer rate from large scale turbulence to small scale turbulence, as shown in the C3 term of (6). In short, (k/ε) is the time scale for small eddies and (k/Π) is the time scale for large eddies, thus the extended k–ε turbulence model [19] has the ability to capture both effects of small and large eddies. A modified wall function approach was employed to provide wall boundary layer solutions that are less sensitive to the near-wall grid spacing. Consequently, the model has combined the advantages of both the integrated-to-the-wall approach and the conventional law-of-the-wall approach by incorporating a complete velocity profile and a universal temperature profile [20]. A 7-species, 9-reaction detailed mechanism [20] was used to describe the finite-rate, hydrogen/oxygen afterburning chemical kinetics. The seven participating species are H_2, O_2, H_2O, O, H, OH, and N_2.

2.2 Nominal 5 s startup sequence

Although the regular hysteresis phenomenon is measured by axial forces, it is conceivable that side force is also driven by memory. That means the transient inlet history has to be modeled as closely as possible to that of the actual hot-fire test. A system model was therefore used to simulate the effect of valve sequencing on inlet history for a nominal 5 s operation. A system model solves conservative, time-varying equations, representing various components and flow passages in a rocket engine, while its database contains empiricism obtained from hundreds of tests. Figure 1 shows some of the inlet flow properties obtained from the system model: the time-varying inlet pressure, temperature, and equivalence ratio profiles. These time-varying inlet properties were used at the injector faceplate of the thrust chamber for the CFD computation. Two significant pressure rise events can be identified in the inlet pressure history of Fig. 1. The first one occurs at 1.5 s due to oxygen prime, while the second one occurs at about 2.4 s, caused by the step opening of the oxygen valves in the pre-burners. The inlet temperature history

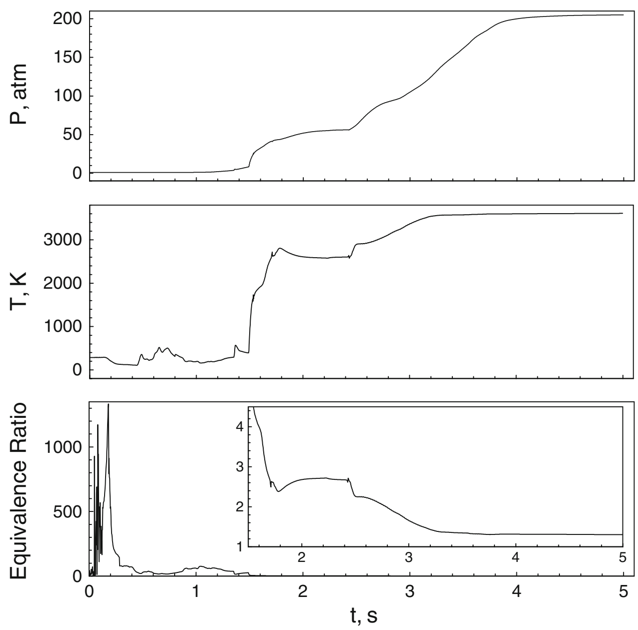

Fig. 1 Simulated thruster inlet properties during the start-up transient

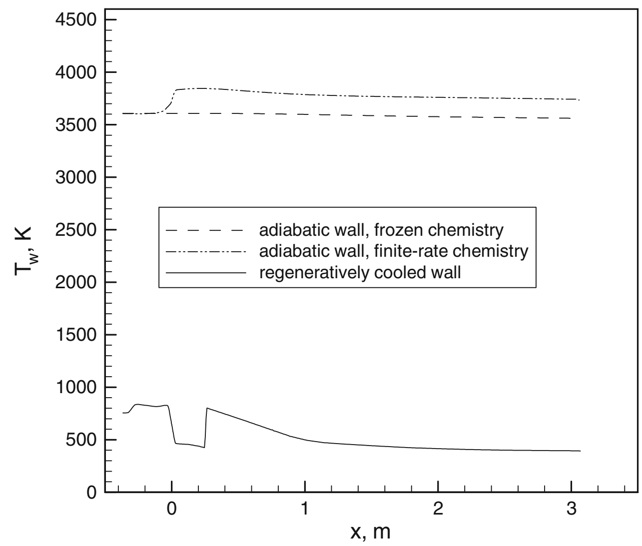

Fig. 2 A comparison of computed axial adiabatic wall temperatures and the regeneratively cooled wall temperature

shows a sharp jump at 1.5 s, leveling off after 1.75 s, jumps a little bit again at 2.4 s, and increases linearly until around 3.1 s when it reaches the final temperature. The inlet equivalence ratio history shows that the thruster environment is fuel rich throughout the start-up transient, especially in the first 1.5 s, setting up the potential for afterburning. That turns out to be the source of the combustion wave, because the pressure jump at 1.5 s increases the reaction rate of afterburning, which leads to the generation of the combustion wave. Afterburning plays an important part in the subsequent asymmetric flow physics such as the shock transitions and shock pulsations across the nozzle lip. As mentioned in the beginning of this section, that the route or history between the starting and end points of any of the curves in Fig. 1 influences the side load physics intimately, any simplification on any part of the sequence may run the risk of missing or degradation of important side load physics.

2.3 Cooled wall temperature distribution for regenerative cooling

It is speculated that wall temperature distribution plays an important role in side load physics, especially for regeneratively cooled walls such as those of the SSME, as a cooled wall was reported to retard flow separation, and a hot wall was reported to promote flow separation [1,13,14]. It is, however, not trivial to obtain a wall temperature distribution, as conjugate heat transfer calculation involving both hot-gas-side and cold-coolant-side flows and their supporting solid structures is required [21]. Especially for a complicated regenerative cooling system such as that employed by SSME, in which the main combustion chamber (MCC) and the nozzle are cooled separately, while the MCC consists of 390 cooling channels and the nozzle has 1,080 cooling tubes. To model that two-way effect of the regenerative cooling transiently, is therefore out of the scope of this effort. A simplified way is to apply a wall temperature distribution to the interior wall, calculated separately through a conjugate heat transfer calculation when nozzle is flowing full, but applying it as the wall thermal boundary condition at an appropriate time into the startup transient, such that the effect of transient cooling is still approximated. Such a cooled wall temperature distribution is obtained and compared with two adiabatic wall temperature profiles, as shown in Fig. 2. The difference between the two calculated adiabatic wall temperatures after the throat ($x = 0$) is caused by the effect of chemistry and composition change. It can be seen that the regenerative cooled wall temperatures are more than 2,500° lower than those of the adiabatic wall, which is significant enough to affect the computed side load physics. Note that for the 3-D transient, adiabatic wall case, the wall temperatures were computed instantaneously and not imposed. That is, only the solid wall wetted by the advancing flow front reaches the adiabatic temperature. For the 3-D transient, cooled wall case, the computation started with the adiabatic wall boundary condition initially, while the axial cooled wall temperature distribution, from Fig. 2, was only imposed at 1.5 s into the startup process, or when the pressure starts to ramp up significantly.

3 Computational grid generation

Parametric studies conducted [15] show that a structured-cell dominated hybrid mesh performed more favorably than an

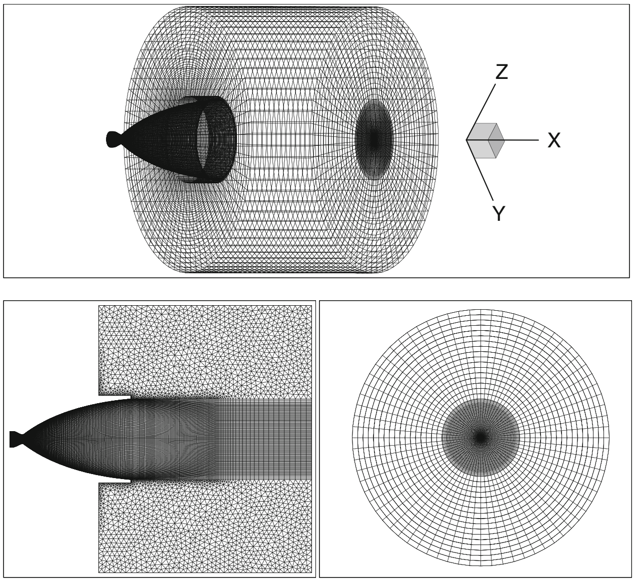

Fig. 3 The layout of hybrid computational grid. *Top* an overall view. *Bottom left* a cross-sectional cut through the nozzle axis. *Bottom right* the exit plane

unstructured-cell dominated hybrid mesh both in accuracy and efficiency, on flow physics and prediction of nozzle design parameters such as axial force and wall heat fluxes. Also, due to the large computational resources required by a transient 3-D computation, it is difficult to perform grid studies on side load applications. That structured-cell dominated hybrid mesh [15] anchored for axial force and wall heat fluxes was therefore employed in this effort, assuming that a grid suitable for axial force calculation is sufficient for side force calculation. As shown in Fig. 3, structured (hexahedral) cells are used in the thruster and bulk plume region, while unstructured (prismatic) elements are used in the freestream region. Since this hybrid computational grid was constructed by rotating a 2-D grid 360° thereby totally symmetric about the x-axis, the computed asymmetric flows are driven solely by the flow physics and not the grid topology. A close-up view of the nozzle interior grid layout can be found in References [15]. The azimuthal discretization between two planes is 5°. The grid density in the structured-grid region is $309 \times 52 \times 73$ in which 309 is the number of points in the axial direction. The grid was generated using a grid generation software package GRIDGEN [22]. The total number of grid points is 1,286,934, or 1,275,120 cells, which is considerably higher than the 85,000 cells used on Vulcain 2 [10], and the 145,500, 145,500, and 405,900 points used on LE-7, LE-7A, and CTP50-R5-L [9], respectively. Note that the SSME nozzle has a thrust optimized contour and its area ratio is 77.5. The good agreement of computed side loads with those of test data reported in latter section, indicates that performing grid studies on axial force and wall heat transfer may be an efficient strategy for nozzle side load applications.

4 Boundary and inlet conditions

Fixed total condition was used for the freestream boundary and a total pressure of 1 atm was used to simulate the nozzle hot-firing at sea level. That freestream boundary condition was designed such that a supersonic plume may go out of the boundary, while the ambient air may come into the boundary due to the possible plume entrainment effect. No-slip condition was specified for the solid walls. The inlet flow properties obtained from the system model simulation include the time varying total pressure, temperature, and propellant composition. The time varying propellant composition was preprocessed with the Chemical Equilibrium Calculation program [23], assuming the propellants were ignited to reach equilibrium composition immediately beyond the injector faceplate. The larger than unity equivalence ratio throughout the 5-s ramp period indicates the SSME is operated at fuel rich condition and the inlet composition contains mostly steam and excess hydrogen. At the start command, or time zero, the entire flowfield was initialized with quiescent air. The presence of air allows the afterburning with the excess fuel which contributes to the side force physics.

5 Results and discussion

The computations were performed on a cluster machine using 12–32 processors. Global time steps were varied throughout the computations: those of 2.5–10 ms were typically used during the initial transient and when the change of flow physics was mild, and those of 1–2.5 ms were used when strong flow physics such as shock transitions and shock pulsations across the nozzle lip were occurring. These time steps correspond to CFL numbers ranging approximately from 0.1 to unity. The results of regeneratively cooled wall case with the nominal 5 s sequence are presented first, then those of the adiabatic wall case with the same nominal 5 s sequence, followed by the results of the second regeneratively cooled wall case using a shortened 1 s sequence. Finally, the computed results are compared with available test data and the associated side load physics interrogated.

5.1 The regeneratively cooled wall case with the nominal 5 s sequence

Figure 4 shows the computed time-varying side loads and associated physics, which, in addition to the nozzle geometry, are uniquely defined by both the cooled wall boundary condition and the nominal 5 s startup sequence. The initial side load after the start command is negligible due to the slow opening valves, yet a core flow is gradually taking shape. At around 0.175 s, that developing core flow becomes a detached core jet, emerging from the throat and comprising mostly steam

Fig. 4 Computed side forces for the cooled nozzle

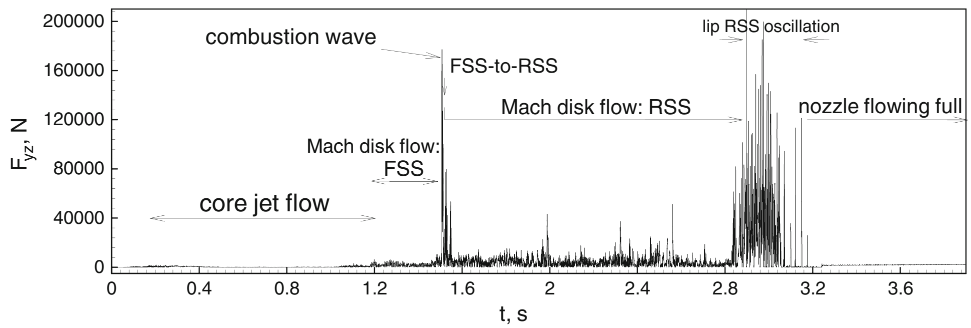

Fig. 5 Computed separation and reattachment lines, and xy-plane Mach number contours showing transition from free-shock separation to restricted-chock separation

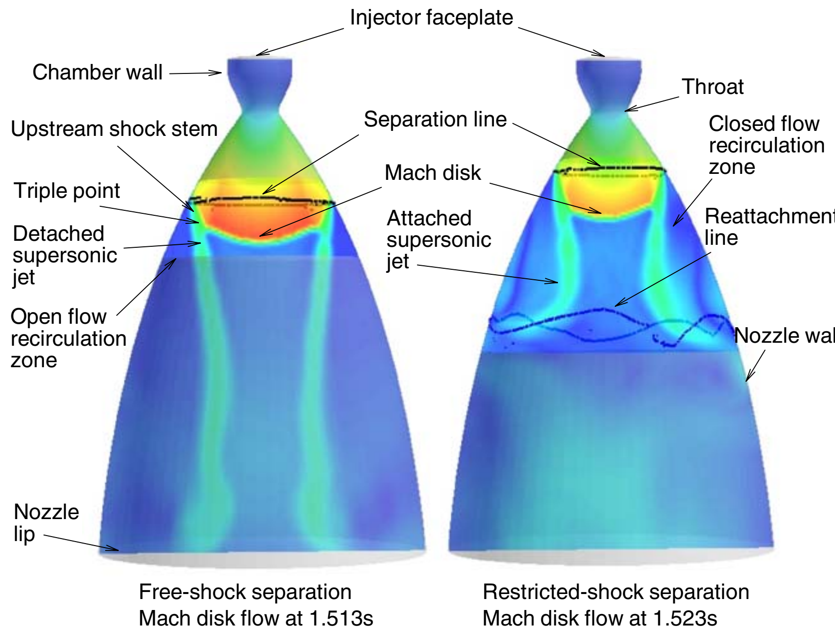

and hydrogen. It gradually gathers speed as the chamber pressure increases. Unlike the flow physics captured in the 2-D planar SSME nozzle [11], where the core jet flow adheres to the wall fairly quickly, creating asymmetric flow and producing early side forces, the core jet flow in the 3-D SSME nozzle is fairly centered, thereby producing negligible side forces during the core jet flow period. It is theorized that the geometrical volume available for air pumping between the core jet and the wall is much larger in a high aspect ratio 3-D nozzle than that of a low aspect ratio 2-D nozzle, hence the difference. At 1.2 s, the core jet chokes to become a Mach disk flow.

As the Mach disk flow develops and the size of the Mach disk grows after 1.2 s, it imposes an adverse pressure gradient in the nozzle. As the wall boundary layer not able to negotiate this adverse pressure gradient due to wall friction, the Mach disk flow stays separated, resulting in an oblique shock foot (stem) coming off the wall, intersecting the Mach disk and a detached supersonic jet at the triple point. Since the detached supersonic jet is flowing freely and away from the wall, this shock and flow separation pattern is named as free-shock separation (FSS) [1,24]. A representative FSS flow pattern is shown in the left plot of Fig. 5—the Mach number contours at 1.513 s into the transient. It is a recovered Mach disk flow after the disruption of a combustion wave, which will be discussed in the next paragraph. It can be seen from the FSS flow pattern in Fig. 5 that an open flow recirculation zone is formed between the nozzle wall, the supersonic jet and the oblique shock which is sometimes referred as an upstream shock foot. There is also a circular and fairly symmetric separation line. The FSS flow pattern shown in Fig. 5 is typical between 1.2 and 1.5 s, where the computed side loads are only slightly larger than those in the core jet flow period.

Going into 1.5 s of the startup transient, there is a lot of excess hydrogen buildup in the nozzle while the chamber temperature rises sharply (see Fig. 1). That leads to afterburning in the mixing layer between the supersonic jet and recirculated air, raising temperature higher, as shown in the first temperature contours at 1.503 s in Fig. 6. The combination of the fuel rich condition and the long residence time of

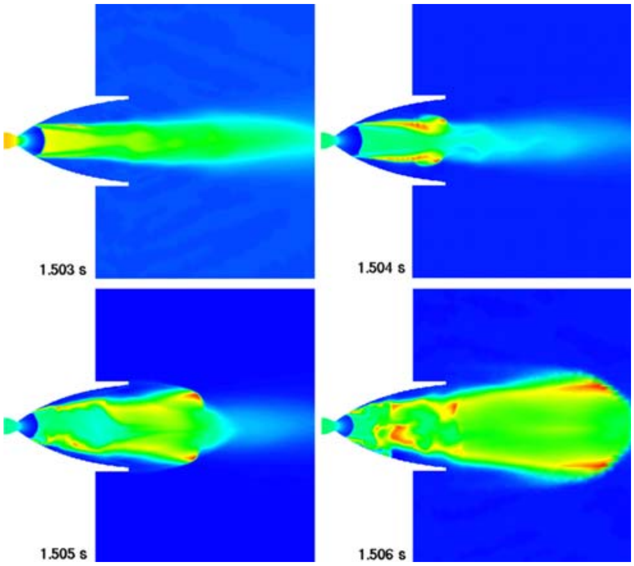

Fig. 6 Computed xz-plane temperature contours of the cooled nozzle showing combustion wave

the nominal 5 s sequence, create a perfect environment for that elevated temperature front to quickly spread through the mixing layer, forming a fast expanding hot gas wave, as indicated in the rest of the temperature contours in Fig. 6. Along side the fast expanding temperature wave, happening simultaneously, is a fast expanding pressure wave (not shown) hereby called combustion wave. It also starts at the mixing layer inside the nozzle while propagating in all directions. The afterburning depletes part of the excess hydrogen and disrupts the Mach disk flow temporarily. In the mean time a portion of the combustion wave moving inside the nozzle inevitably hits the wall. The combination of both incurs the first significant side load (see Fig. 4) and several smaller ones thereafter due to shock reflections, while the rest expands away.

Soon after the disappearance of the combustion wave, the partially depleted hydrogen-rich Mach disk flow recovers and soon resumes its FSS mode, as shown in the left plot of Fig. 5. Since the inflow is still fuel rich, afterburning continues, causing the Mach disk to move back and forth, as the Mach disk flow moving downstream due to the increasing chamber pressure, while constantly adjusting itself to the expanding nozzle flow area. Simultaneously the supersonic jet fluctuates, sometimes closing in onto the wall. All of these physical movements combine to create a slight pressure imbalance and thereby pumping action. At a certain point the pumping becomes large enough to cause another physical change of the Mach disk flow. That is, the free-flowing supersonic jet of the FSS starts to move towards the nozzle wall at around 1.520 s, and just attaches itself to the wall at 1.523 s to form a closed flow recirculation zone, as shown in the right Mach number contours of Fig. 5.

When the supersonic jet of the Mach disk flow restricts itself to attaching the wall, the shock and flow separation pattern is aptly named as the restricted-shock separation (RSS) [1,24]. The transition from the Mach number contours at 1.513 s to that at 1.523 s in Fig. 5 is called the FSS-to-RSS transition. It can be seen from Fig. 5 that when the supersonic jet is just fully attaching to the wall, the shape of the reattachment line is not circular, but resembling an asymmetric petal, exhibiting strong three-dimensionality. The transition from a rather symmetric wall pressure distribution of FSS at 1.513 s to an asymmetric wall pressure distribution of RSS at 1.523 s represents a large pressure disturbance, causing another large side load jump, as shown in Fig. 4.

The mechanism of the free flowing supersonic jet adhering to the wall can be traced back to the classical Coanda effect [25,26]. In 1936, Coanda found when a jet or sheet of fluid issues into another fluid, the velocities of the turbulently moving particles are greater than the jet speed, thus creating under pressure and a suction effect, drawing the surrounding fluid into the jet. If there is a wall nearby, the space between the jet and adjacent wall becomes evacuated and the jet tends to stick to the nearest surface. Since the supersonic jet of a FSS flow pattern is essentially a hollow, tubular sheet of fluid, the pumping action and the eventual sticking of the supersonic jet to the wall to become a RSS flow pattern are perfectly explainable by the Coanda effect.

After the FSS-to-RSS transition at 1.523 s, the remaining of the supersonic jet continues to attaching to the wall and the recirculation bubble shrinks, producing several smaller side load jumps, until around 1.530 s, as shown in Fig. 4. Eventually the recirculation bubble size stabilizes, and the unattached part of the supersonic jet becomes the downstream shock stem or foot. At that moment, the upstream shock stem, the downstream shock stem, and the Mach disk form a so-called Lambda shock. The reattachment line is now more symmetric, and the RSS Mach disk flow continuously walks down the nozzle wall with its two shock feet, until the downstream foot reaches the nozzle lip at around 2.875 s, as indicated in Fig. 4, while all the time the Mach disk and its two feet are oscillating back and forth due to the afterburning reactions, producing occasional mild side load jumps that are lower in magnitude than that of the FSS-to-RSS transition.

Between 2.875 and 3.15 s inside the startup transient, a unique side-load phenomenon was computationally captured for the first time. That is, the two-footed RSS Mach disk flow was computed to be pulsating or breathing in-and-out of the nozzle lip several tens of times [1,24]. The previously symmetric two-footed RSS Mach disk flow now goes asymmetric while crossing the nozzle lip, especially during the retracting portion of the pulsation when the shock wave moves helically. This can be seen from Fig. 7 where the xz-plane Mach number contours show a slanted Mach disk with asymmetric shock stems, resulting in a fatter and shorter supersonic jet

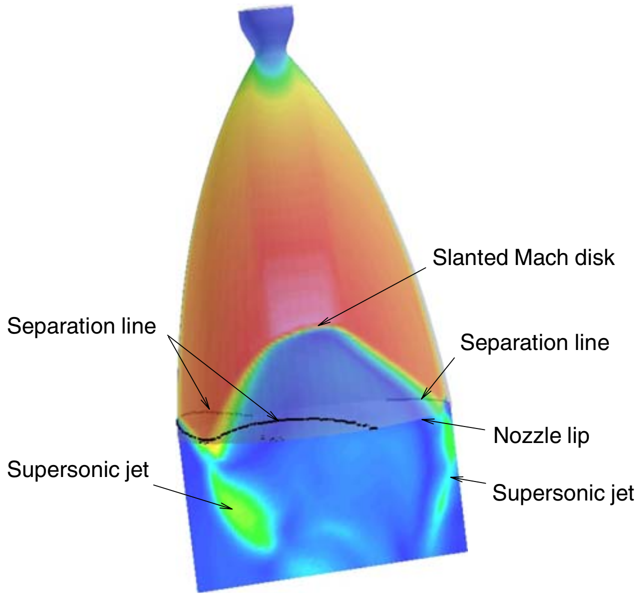

Fig. 7 Computed xz-plane Mach number contours and separation line for the cooled nozzle during a retracting portion of the shock pulsation across the lip at 3.099 s

on the left-hand side and a thinner and longer supersonic jet on the right-hand side. In addition, two teepee-like shocks marked by separation line appear above the nozzle lip, indicating the upstream shock foot (stem) on the left-hand-side has back-stepped into the nozzle at two places. In the mean time, the upstream shock foot on the right-hand-side is just about to back-step into the nozzle, evidenced by a small section of separation line right on the nozzle lip. It can be seen that this is a much more asymmetric and 3-D shock pattern than that of the FSS-to-RSS transition shown in Fig. 5. In addition, unlike the FSS-to-RSS transition and combustion wave that happen only once at a location of small area ratio, this asymmetric side load physics repeat itself several tens of times and occur near the nozzle lip where the aspect ratio is at maximum, resulting in several tens of very large side load jumps for a long period of time or 0.275 s, as shown in Fig. 4. This RSS pulsation across the nozzle lip is therefore the most important side load event, more important than the events of combustion wave and FSS-to-RSS transition due to its sheer magnitude and duration. After 3.15 s, the nozzle is flowing full and the side load drops to negligible value, as expected.

5.2 The adiabatic wall case with the nominal 5 s sequence

Next, we examine results of the adiabatic wall case with the nominal 5 s sequence. Figure 8 shows the computed time-varying side loads and associated physics. It can be seen that similar to the regeneratively cooled wall case, the combustion wave and FSS-to-RSS transition were also captured, except the side load due to combustion wave is higher because of the implied energy loss in the cooled nozzle. The difference in side load physics between the two wall boundary conditions starts after the first FSS-to-RSS transition. That is, for the adiabatic nozzle, after the FSS-to-RSS transition, the RSS flow pattern lasted only 0.03 s, after which RSS-to-FSS transition occurs (at 1.524 s), producing a side load jump slightly higher than that of the FSS-to-RSS transition, and the Mach disk flow stays at FSS mode until around 2.4 s. This phenomenon may be explained by reviewing and contrasting the result of the cooled wall transient after the FSS-to-RSS transition, where the RSS flow pattern stays throughout this part of the transient until the downstream shock foot reaches the nozzle lip. That is, with a regeneratively cooled wall, density is higher in the wall boundary layer. That leads to higher turbulent eddy viscosity, higher momentum, thinner boundary layer and lower pressure. That lower pressure works like an extra suction force, in addition to that of the original Coanda effect on the supersonic jet side, ensuring the supersonic jet to stay adhering to the wall. On the other hand, with the adiabatic wall, since the overall temperature of the just closed recirculation zone is much higher than that of the cooled wall, especially near the separation and reattachment lines where the stagnation temperature rules, the opposite is true. There is now an opposing force large enough to push the supersonic jet off the wall, and to stay off. Thus, the regeneratively cooled wall promotes the Coanda effect, while the hot adiabatic wall fights off the Coanda effect. These computed flow physics agree with those reported in References [1,13,14] in which thinner, cold-wall boundary was found to be less susceptible to separation than was the hot-wall. Note that since the supersonic jet of the RSS flow pattern reattaches itself after the reattachment line, it may be viewed as less separated than the fully separated FSS flow pattern.

Between 1.524 and 2.4 s, the supersonic jet of the exhausting FSS Mach disk flow flaps, or fish tails, trying to become attached, to no avail, due to the anti-Coanda effect of the hot wall. But with the second pressure rise event occurring after 2.4 s, the intensity of the fish tailing increases and the supersonic jet finally attaches to the wall, albeit briefly, forming the simultaneous FSS and RSS, or partial RSS flow pattern. In particular, there are FSS ↔ 1/4 RSS transitions between 2.425 and 2.8 s, as indicated in Fig. 8. The "1/4 RSS" flow pattern means the attached region covering about a quarter of the circumference, while the rest of the region is detached. The FSS ↔ 1/4 RSS transitions represent many a back-and-forth modulations between FSS and 1/4 RSS flow patterns. Figure 9 shows a snapshot of a typical 1/4 RSS flow pattern in which the xz-plane Mach number contours show a FSS flow pattern, but the xy-plane contours indicate an attached supersonic jet in the lower portion of the Mach disk flow, at 2.625 s into the transient. Again, the shock stem from the Mach disk side, the upstream shock foot, triple point,

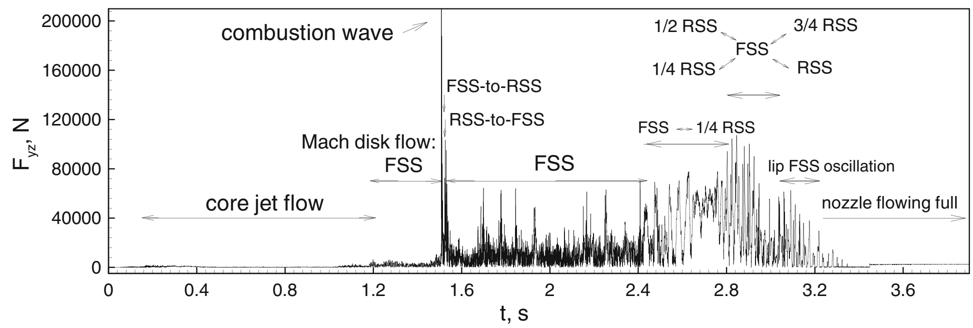

Fig. 8 Computed side forces for the adiabatic nozzle

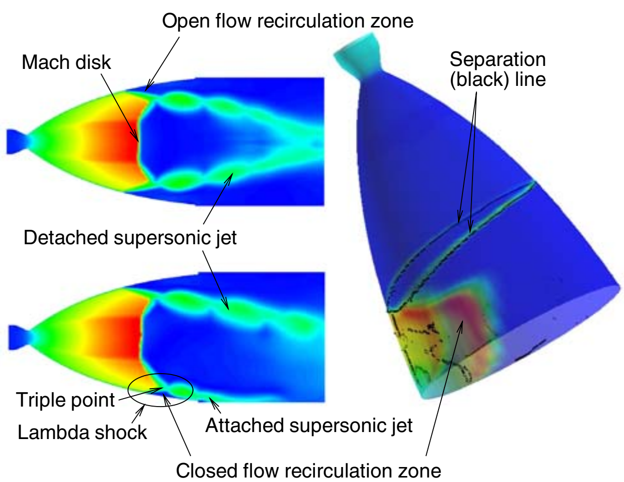

Fig. 9 Computed scalar contours of the adiabatic nozzle at 2.625 s. *Top left* Mach number contours on xz-plane. *Bottom left* Mach number contours on xy-plane. *Right* wall OH concentration contours and separation line

and the attached supersonic jet (downstream foot) constitute a Lambda shock formation, although only partially in the circumferential sense. The 1/4 RSS flow pattern is asymmetric therefore generating higher side loads than those of pure FSS flow pattern occurring prior to 2.4 s.

Figure 9 also shows the wall OH concentration contours along with the separation line. Higher OH concentration often indicates higher reaction rate and higher local temperature. It can be seen that the visible OH concentration contours composed of two parts: the upper part shapes like a slanted plane that overlays with the upper part of the separation line; while the lower part represents the flow recirculation region and coincides with the separation line that also bounds the recirculation bubble. This is because the afterburning reaction rate is higher in the recirculated flow region and at the separation line where the temperatures are high. Plotting OH concentration contours is therefore an alternative way of indicating separation line and recirculated flow region, but clearly OH concentration contours have more physical meaning than that of the separation line. Note the slanted plane in Fig. 9 closely resemble the so-called "tilted plane" as described in Nave and Coffey [1], which is the basis of several empirical side load prediction approaches. It needs to be pointed out though, when there is a slanted (separation) plane, there is the associated recirculation bubble which is not represented by the "tilted plane" methods.

After 2.8 s, the fish-tailing activity of the FSS intensifies even more and we have random transitions from FSS to various kinds of partial RSS flow patterns, as shown in Fig. 8, and the side loads jump even higher than those between 2.4 and 2.8 s. Then the fish-tailing activity drops off as the single shock foot of the FSS reaches the nozzle lip at around 3.04 s. Between 3.04 and 3.22 s, the FSS Mach disk flow pulsates many times in-and-out of the nozzle lip, but the resulting side loads are much lower than those of the RSS Mach disk flow breathing across the lip. This is anticipated because the pressure disturbance caused by the single shock foot should be less than that of the two shock feet. After 3.22 s, the adiabatic nozzle flows full.

5.3 The regeneratively cooled wall case with the 1 s sequence

The impact of nozzle side loads is often countered with strengthening the nozzle structure, with added penalty of increased weight, which may be avoided if ways can be devised to reduce the nozzle side loads. One of the common parameter linking the aforementioned three asymmetric shock evolutions, i.e., the occurrence of combustion wave, shock transitions, and shock pulsations across the nozzle lip, appears to be the ramp rate which relates closely with the ramp time. That is, the magnitude and duration of the various side load events are not only a function of the chamber pressure for example, but also a function of the rate of change of the chamber pressure when a specific side load event is happening. The nominal 5 s ramp time has long been suspected as too long, and that a shorter ramp time, or higher ramp rate may be effective in reducing the side loads. The cooled wall case with a 1 s startup sequence was therefore performed. This 1 s startup sequence was achieved by taking the transient inflow properties of the nominal 5 s sequence shown in Fig. 1 and reducing the total ramp time from the 5

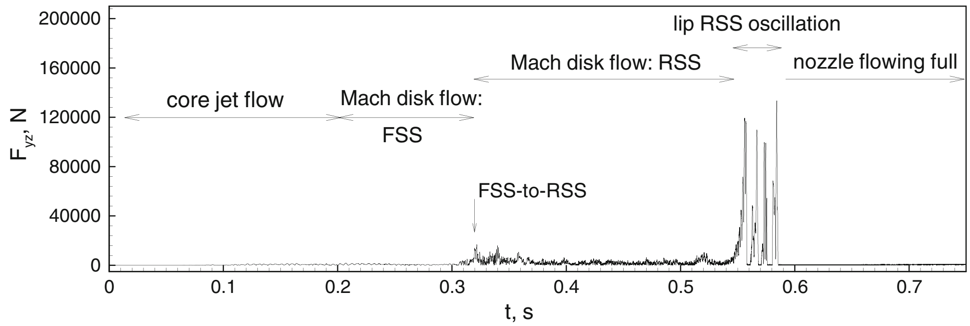

Fig. 10 Computed side load for the cooled wall case with a 1 s sequence

to 1 s. That means the ramp rate of this 1 s sequence is five times faster than that of the nominal 5 s sequence.

Figure 10 shows the computed side load history for the regeneratively cooled wall with the aforementioned 1 s total ramp time. Comparing to the side load history for the regeneratively cooled wall case with the nominal 5 s startup sequence, it can be seen that qualitatively they look similar, but there are major differences in terms of the side loads produced by the three shock evolutions in the 5 s sequence. First, the side load due to combustion wave vanishes. That is because the ramp time is so short that there is not enough residence time for the afterburning to be taken to a higher level, thus the occurrence of the combustion wave is avoided. Second, the side load jump caused by the FSS-to-RSS transition is lower than that of the 5 s sequence. That too can be explained by the shortening of the elapsed time for the FSS transitioning to RSS, which in turn shortens the asymmetric flow time and its consequence. Finally, the peak side load caused by the RSS pulsation across the nozzle lip is also much lower than that of the 5 s sequence. And once again it is explained by the curtailing of the afterburning residence time and the pulsation time due to the higher ramp rate, which limits the helical motion and amplitude of the pressure disturbances. The reduction of the pulsation time also decreases the number of shock pulsations across the nozzle lip, which significantly reduces the impact of the RSS pulsation on the nozzle structure. This result indicates that if a shorter ramp time is feasible, the side loads induced by the three shock evolutions could be eliminated or reduced.

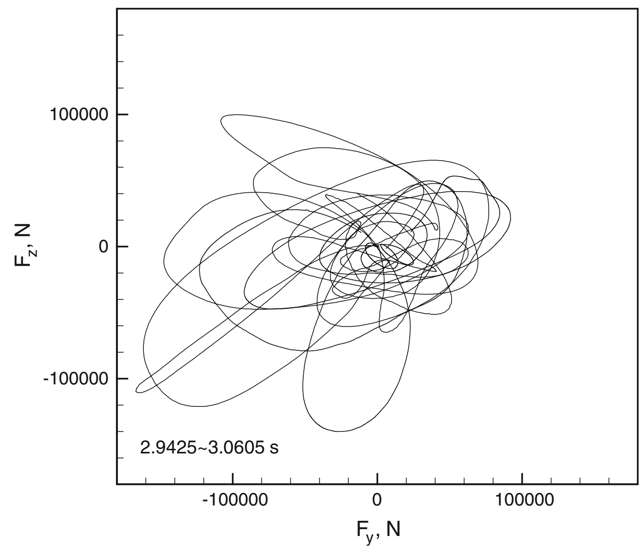

Fig. 11 Computed side force locus for the cooled nozzle

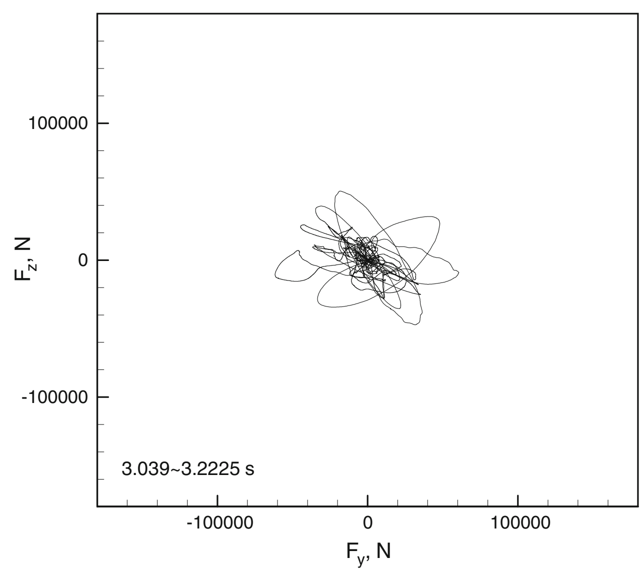

Fig. 12 Computed side force locus for the adiabatic nozzle

5.4 Comparison of computational results with those of tests

For both the adiabatic and cooled nozzles with the nominal 5 s startup sequence, the shock pulsations across the nozzle lip show helical motion (or tangential movement when projected to the 2-D yz-plane) with the side force locus, especially during the retracting part of the pulsation. These tangential movements are presented as 2-D polar plots, and shown in Figs. 11 and 12, respectively. The side force vector moves counter-clockwise (looking into the nozzle) during these tangential movements. It can be seen that the radii of the side force locus of the adiabatic nozzle is much restricted and centered around the origin, while the radii of that for the regeneratively cooled nozzle cover significantly more ground and

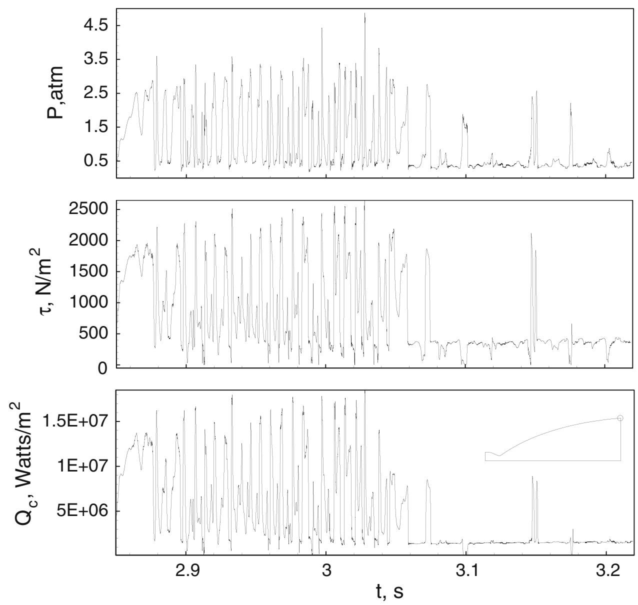

Fig. 13 Computed near lip wall pressure, shear stress, and heat flux histories for the cooled nozzle

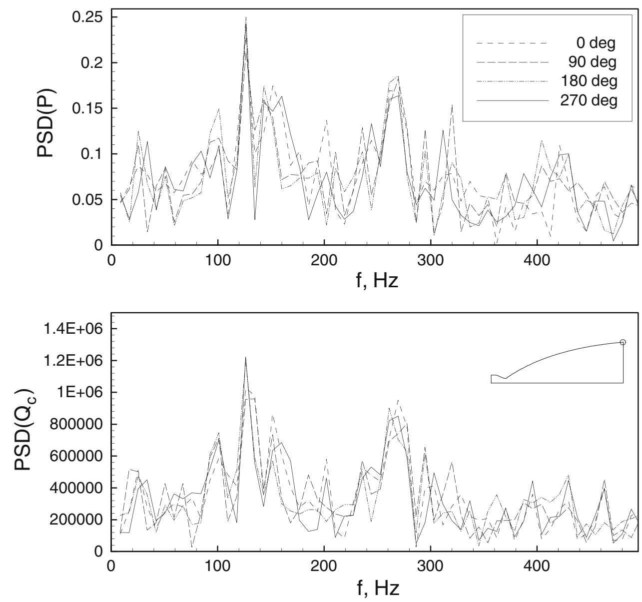

Fig. 14 Computed frequency domain for the cooled nozzle

Table 1 A comparison of dominant frequencies

	Dominant frequency (Hz)	Variable
Adiabatic nozzle	45	Pressure
	49	Temperature
Cooled nozzle	122	Pressure
	125	Heat flux
Test data	120	Pressure

appear to be biased toward the lower-left quadrant, revealing that the regeneratively cooled nozzle incurs more asymmetric flow, higher peak side load, and stronger tangential movement than those of an adiabatic nozzle. Since the stronger tangential movement tends not to center around the geometrical center of the nozzle, as a result, teepee-like structure (see Fig. 7) was captured with the regeneratively cooled nozzle, but not computed with the adiabatic nozzle. The tangential teepee movements were observed during both the SSME and J2S [1] hot-firings.

As the Mach disk flow pulses in and out of the nozzle exit plane, it is actually the shock legs moving in and out of the last part of the nozzle, resulting in pressure oscillations and generating side forces as shown in Fig. 4. Figure 13 shows the computed wall pressure, shear stress, and heat flux histories for the regeneratively cooled nozzle at a monitoring point near the nozzle lip. Those monitored at the same axial location but circumferentially away from this point by 90°, 180°, and 270° are qualitatively similar to these and are not shown. As mentioned above, with the Mach disk wave pulsating in-and-out of the nozzle, these flow properties fluctuate as the shock legs passing back-and-forth by the monitoring point. Since gas temperature, density, and pressure are related by the equation of state, it is not surprising that the fluctuating histories of the wall pressure, shear stress and heat flux look qualitatively similar. In addition, the fact that the heat flux history appears to correlate with those of pressure and shear stress suggesting the transient thermal load may also play a role in terms of thermal stress. This is supported by the reported damage to some regenerative cooling tubes by strong heat-load during the startup and shutdown processes in early LE-7A engine development, by Watanabe et al. [27].

Examining the fluctuating histories in Fig. 13 closely, it can be seen that the frequencies of the fluctuations start rather slowly, reach an approximate constant between 2.9 and 3 s, then slow down after 3 s, and really slow down after 3.05 s. Hence, by clipping out the slower frequencies at both ends, a series of Fourier analyses were performed for the pressure and heat flux histories between 2.90375–3.0225 s for all four monitoring points, such that dominant frequencies may be obtained to compare with those acquired from a subscale test. The result is presented as power spectral density profiles, as shown in Fig. 14. The dominant frequency based on the pressure is about 122 Hz, while that based on the heat flux is about 125 Hz, demonstrating the fluctuating frequencies between pressure and heat are indeed similar. The same Fourier analyses were performed with computed wall pressure and temperature histories for the adiabatic nozzle between 3.04 and 3.2225 s. The dominant frequency based on pressure is about 45 Hz, while that based on temperature is slightly higher at about 49 Hz. These results are summarized in Table 1. The test data of 120 Hz was scaled to the full

Table 2 A comparison of local peak side loads

F_{yz} (kN)	Test	Computation		
		Adiabatic nozzle	Cooled nozzle	Responsible side load physics
–	–	395	176	Combustion wave
Secondary	90	70	80	FSS-to-RSS transition
		102	–	RSS-to-FSS transition
Primary	200	110	–	FSS-to-partial RSS transition
		60	–	FSS pulsation across lip
		–	212	RSS pulsation across lip

scale SSME test conditions from a subscale SSME nozzle air flow test [28]. It can be seen that the dominant frequencies arrived from the regeneratively cooled nozzle agree reasonably well with that of the test, while those of the adiabatic nozzle are more than 50% too low. It should be noted that while the low frequency lip oscillations are caused predominantly by the movement of the shock legs in-and-out of the nozzle lip, as discussed previously, large vortices or eddies associated with the openings and closings of the shock legs occur. The interaction of the shock legs with the large eddies near the lip may have contributed to the teepee-like separation line shown in Fig. 7, aptly captured by the extended k–ε turbulence model [19] that models both the small and large eddies.

Table 2 shows a comparison of the computed local peak side loads with the associated physics, and those from a hot-firing test. The test measured two local peak side loads. The first or secondary side load of 90 kN occurs right after the first pressure-rise event, while the second or primary side load of 200 kN happening around 3 s into the nominal 5 s sequence. It can be seen that the computed local peak side load of 70 kN due to FSS-to-RSS transition and that of 102 kN due to RSS-to-FSS transition of the adiabatic nozzle, and that of 80 kN due to FSS-to-RSS of the cooled nozzle, are all agree reasonably well with the measured secondary peak side load, and all of which happen after the first pressure rise event. The physics of the measured first local peak side load is therefore associated with the shock transitions. The computed side loads due to combustion wave happen slightly ahead of the shock transitions, but do not appear to be measured by the test. This is because precautionary measures such as the sparklers (not simulated in this study) were placed near the nozzle exit to burn off excess fuel flowing into the nozzle (see the equivalence ratio plot in Fig. 1), the combustion wave induced side loads were therefore avoided. Flame torches are also often used during hot-firing test of rocket engines for the same purpose.

The computed maximum side load of 212 kN due to the RSS pulsation across the regeneratively cooled nozzle lip agrees quite well with that of the measurement, and the timing of its occurrence also matches with that of the test. For the adiabatic nozzle, however, the timing of the occurrence of the FSS-to-partial RSS transitions is slightly early and its magnitude of 110 kN is about 50% lower than the 200 kN of the test; in addition, the local peak side load of 60 kN due to the FSS pulsation across the nozzle lip is 70% lower than the 200 kN of the test. The physics of the SSME primary side load is therefore associated with the RSS pulsation across the nozzle lip. Note the measured primary peak side load of 200 kN is more than twice the magnitude of that of the secondary peak side load.

Contrary to the results [15] that cooled wall boundary condition gives lower axial force (thrust) than that of adiabatic wall because of the energy loss, the regeneratively cooled nozzle produces much higher peak side force and pulsation frequency than those of the adiabatic nozzle. This is because the cooled wall promotes the Coanda effect, causing the supersonic jet to stay attached, thereby maintaining the RSS flow pattern after the FSS-to-RSS transition. On the other hand, the adiabatic wall fights off the Coanda effect, repelling the supersonic jet off the wall to stay detached most of the time. As a result, the two-legged RSS pulsation across the nozzle lip produces much higher wall pressure disturbance and pulsation frequency, than those of the one-legged FSS pulsation across the nozzle lip. These benchmarks indicate that the cooled wall boundary condition performs more favorably than that of the adiabatic wall for a regeneratively cooled engine such as the SSME.

6 Conclusions

A unique computational methodology based on a pressure-based CFD and heat transfer formulation, and a system modeling for the transient inflow properties, was developed to predict the aerodynamic side load for regeneratively cooled, high aspect ratio nozzles. The computational methodology was anchored by simulating the full-scale SSME startup transient at sea level, with emphases putting on the wall thermal boundary conditions and ramp time. Three types of shock evolution were computed to generate significant side loads that could cause hardware damages: the occurrence of combustion wave, shock transitions, and shock pulsations across the nozzle lip, although the side load induced by combustion wave can be avoided by installing excess fuel burning devices, such as sparklers or flame torches. It is found that the afterburning plays an important role in all of the side load physics, while the Coanda effect helps drawing the supersonic jet to the wall thereby contributing to the circumstance of FSS-to-RSS transition. The cooled wall boundary condition then further promotes the Coanda effect to favor the RSS flow pattern, while the adiabatic wall boundary condition fends off the Coanda effect to prefer the FSS flow pattern. As a result, the computed peak side load due to RSS pulsation across the nozzle lip and the associated dominant pulsation frequency of the cooled wall nozzle agree reasonably well with the measured peak side load and the pulsation frequency of the tests, respectively. However, the computed peak side load due to FSS-to-partial RSS transitions and FSS pulsation across the nozzle lip and the associated dominant pulsation frequency of the FSS pulsation are too low when compared to those of the tests, respectively. Hence, although both boundary conditions predicted secondary side loads associated with shock transitions match that of the data, the peak side load comparisons demonstrated that the cooled wall boundary condition is a more realistic treatment than that of the adiabatic wall, for a regeneratively cooled engine. In addition, when the ramp time is proportionately shortened from the nominal 5 to 1 s, not only is the combustion wave eliminated, but the side loads induced by the shock transition and the shock pulsation across the nozzle lip are also much lower than those of the nominal 5 s sequence, making the shortened ramp time a potentially effective way in transient nozzle side load reduction. Finally, since the side load induced by the shock transitions is considerably lower than that of the RSS pulsation across the nozzle lip, while that incurred by the combustion wave can be eliminated by auxiliary devices, the long enduring RSS pulsation across the nozzle lip along with its associated helical shock motion appear to be the dominant side load physics for a regeneratively cooled, high-aspect-ratio rocket engine.

Acknowledgments This study was partially supported by a Marshall Space Flight Center effort entitled "Nozzle Side Load Technology". The author wishes to thank Chief Aerodynamicist Werner Dahm for his guidance, and Dave Seymour for providing result from engine system simulation. Y.-S. Chen of Engineering Sciences Inc. provided valuable technical support and discussions. James Beck of Rocketdyne Boeing provided test observations on SSME side load physics. Discussions with Joe Ruf on side load physics, and with Daniel Dorney, and Kader Frendi of University of Alabama at Huntsville on frequency analysis are also acknowledged.

References

1. Nave, L.H., Coffey, G.A.: Sea level side loads in high-area-ratio rocket engines. AIAA Paper 73-1284, Reston, VA (1973)
2. Cikanek, H.A.: Characteristics of space shuttle main engine failures. AIAA Paper 87-1939, Reston, VA (1987)
3. Brown, A.M., Ruf, J., Reed, D., D'Agostino, M.D., Keanini, R.: Characterization of side load phenomena using measurement of fluid/structure interaction. AIAA Paper 2002-3999, Reston, VA (2002)
4. Winterfeldt, L., Laumert, B., Tano, R., Geneau, J.F., Blasi, R., Hagemann, G.: Redesign of the Vulcain 2 nozzle extension. AIAA Paper 2005-4536, Tucson, AZ (2005)
5. Watanabe, Y., Sakazume, N., Tsuboi, M.: LE-7A engine nozzle problems during the transient operations. AIAA Paper 2002-3841, Reston, VA (2002)
6. Hagemann, G., Terhardt, M., Frey, M., Reijasse, P., Onofri, M., Nasuti, F., Ostlund, J.: Flow separation and side-loads in rocket nozzles. In: 4th International Symposium on Liquid Space Propulsion, March 12–15, DLR Lampoldshausen (2000)
7. Wang, T.-S.: Numerical study of the transient nozzle flow separation of liquid rocket engines. Comput. Fluid Dyn. J. **1**, 319–328 (1992)
8. Chen, C.L., Chakravathy, S.R., Hung, C.M.: Numerical investigation of separated flows. AIAA J. 32:1836–1843 (1994). doi:10.2514/3.12181
9. Yonezawa, K., Yokota, K., Tsujimoto, K., Sakazume, N., Watanabe, Y.: Three-dimensional unsteady flow simulation of compressed truncated perfect nozzles. AIAA Paper 2002-3991, Reston, VA (2002)
10. Boccaletto, L., Lequette, L.: CFD computation for rocket engine start-up simulation. AIAA Paper 2005-4438, Reston, VA (2005)
11. Wang, T.-S.: Transient two-dimensional analysis of side load in liquid rocket engine nozzles. AIAA Paper 2004-3680, Reston, VA (2004)
12. Tomita, T., Sakamoto, H., Onodera, T., Sasaki, M., Takahashi, M., Tamura, H., Watanabe, Y.: Experimental evalualtion of side-load characteristics on TP, CTP, and TO nozzles. AIAA Paper 2004-3678, Reston, VA (2004)
13. Chang, C.L., Kronzon, Y., Merkle, C.L.: Time-iterative solutions of viscous supersonic nozzle flows. AIAA J. **26**, 1208–1215 (1988). doi:10.2514/3.10030
14. Shimura, K., Asako, Y., Lee, J.H.: Numerical analysis for supersonic flows in a cooled nozzle. Numer. Heat Transf. **26**,631–641 (1994). doi:10.1080/10407789408956014
15. Wang, T.-S.: Multidimensional unstructured-grid liquid rocket engine nozzle performance and heat transfer analysis. J. Propuls. Power **22**, 78–84 (2006). doi:10.2514/1.14699
16. Shang, H.M., Chen, Y.-S.: Unstructured adaptive grid method for reacting flow computation. AIAA Paper 1997-3183, Seattle, WA (1997)
17. Wang, T.-S., Chen, Y.-S., Liu, J., Myrabo, L.N., Mead Jr., F.B.: Advanced performance modeling of experimental laser lightcraft. J. Propuls. Power **18**, 1129–1138 (2002). doi:10.2514/2.6054
18. Chang, G., Ito, Y., Ross, D., Chen, Y.-S., Zhang, S., Wang, T.-S.: Numerical simulations of single flow element in a nuclear thermal thrust chamber. AIAA Paper 2007-4143, Miami, FL (2007)
19. Chen, Y.-S., Kim, S.W.: Computation of turbulent flows using an extended $k-\varepsilon$ turbulence closure model. NASA CR-179204 (1987)
20. Wang, T.-S., Droege, A., D'Agostino, M., Lee, Y.-C., Williams, R.: Asymmetric base-bleed effect on X-33 aerospike plume induced base-heating environment. J. Propuls. Power **20**, 385–393 (2004). doi:10.2514/1.10385

21. Wang, T.-S., Luong, V.: Hot-gas-side and coolant-side heat transfer in liquid rocket engine combustors. J. Thermophys. Heat Transf. **8**, 524–530 (1994). doi:10.2514/3.574
22. Steinbrenner, J.P., Chawner, J.R., Fouts, C.: Multiple block grid generation in the interactive environment. AIAA Paper 90-1602, Reston, VA (1990)
23. Svehla, R.A., McBride, B.J.: FORTRAN IV computer program for calculation of thermodynamic and transport properties of complex chemical systems. NASA TN D-7056 (1973)
24. Nguyen, A.T., Deniau, H., Girard, S., De Roquefort, T.A.: Unsteadiness of flow separation and end-effects regime in a thrust-optimized contour rocket nozzle. Flow Turbul. Combus. **71**, 161–181 (2003). doi:10.1023/B:APPL.0000014927.61427.ad
25. Coanda, H.: Device for deflecting a stream of elastic fluid projected into an elastic fluid. US Patent # 2,052,869, 1936
26. Kumada, M., Mabuchi, I., Oyakawa, K.: Studies on heat transfer to turbulent jets with adjacent boundaries. Bull. Jpn Soc. Mech. Eng. **16**, 1712–1722 (1973)
27. Watanabe, Y., Sakazume, N., Yonezawa, K., Tsujimoto, Y.: LE-7A engine nozzle flow separation phenomenon and the possibility of RSS suppression by the step inside the nozzle. AIAA Paper 2004-4014, Reston, VA (2004)
28. Larson, E.W., Ratekin, G.H.: Structural response to the SSME fuel feedline to unsteady shock oscillations. Shock Vib. Bull. Bull. **52**(Part 2), 177–182 (1982)